ACCSCIENCE PUBLISHING

International Journal of Bioprinting

RESEARCH ARTICLE

Dual-strategy modification for three-dimensional-printed silk methacryloyl hydrogels: Nanofiber reinforcement and poly(ethylene oxide)-induced porosity

Bingxue Xv†, Xin An†, Ning Zhou, Wenxin Meng, Yvmeng Luo, and Guomin Wu*

College & Hospital of Stomatology, Anhui Medical University, Key Lab. of Oral Diseases Research of Anhui Province, Hefei 230032, China.

Abstract

Hydrogels have emerged as promising scaffolds for cartilage tissue engineering due to their structural mimicry of native articular cartilage extracellular matrix. However, conventional hydrogels typically exhibit only nanoscale porosity and poor mechanical properties, which limit nutrient delivery, metabolic waste exchange, and structural fidelity. To address these challenges, we developed an innovative cell-laden porous silk methacryloyl (SilMA) hydrogel system with biomechanical reinforcement using three-dimensional (3D) bioprinting. The porous architecture was created through a water-in-water emulsification strategy employing poly(ethylene oxide) (PEO) as a sacrificial template. This pore-forming process resulted in a remarkable structural modulation, achieving an increase of over 100% in average pore diameter and a 75% enhancement in overall porosity compared to hydrogels without PEO. However, this structural modification compromised the compressive modulus by approximately 50%. Therefore, homogenized electrospun silk fibroin nanofibers (NFs) were incorporated into the bio-ink to improve the mechanical properties and optimize surface topography. The introduction of NFs (1–2 wt%) not only recovered the compressive strength and modulus (close to SilMA hydrogels) but also improved the 3D printability of PEO/SilMA hydrogels. Additionally, the hydrogel demonstrated excellent biocompatibility and markedly upregulated expression of chondrogenic-related genes, including *COL2A1*, *ACAN*, and *SOX9*. Furthermore, the subcutaneous implantation experiments in non-obese diabetic/severe combined immunodeficiency mice further confirmed the potential of PEO/NF/SilMA hydrogels in promoting cartilage formation. Therefore, this study proposes a promising dual-strategy approach for cartilage tissue engineering, integrating NFs reinforcement and PEO-induced porosity.

Keywords: Cartilage regeneration; Electrospun nanofiber; Poly(ethylene oxide); Silk methacryloyl; Three-dimensional bioprinting.

†These authors contributed equally to this work.

***Corresponding author:**
Guomin Wu
(wuguomin@ahmu.edu.cn)

Citation: Xv B, An X, Zhou N, Meng W, Luo Y, Wu G. Dual-strategy modification for three-dimensional-printed silk methacryloyl hydrogels: Nanofiber reinforcement and poly(ethylene oxide)-induced porosity. *Int J Bioprint*. 2025;11(4):278-296. doi: 10.36922/IJB025140118

Received: April 1, 2025
1st revised: May 10, 2025
Accepted: May 19, 2025
Published Online: May 19, 2025

1. Introduction

Articular cartilage injuries caused by aging, obesity, occupational injury, and trauma often develop into osteoarthritis, a leading cause of disability worldwide. While approximately 300 million people were affected in 2019, this number surged to 3.53 billion by 2021.[1] Articular cartilage is a highly hydrated connective tissue devoid of nerves, blood vessels, and lymphatic vessels, consisting primarily of chondrocytes and dense extracellular matrix (ECM).[2] These histological structural characteristics limit its self-repair capacity, placing a substantial burden on the global healthcare system and economy. In response, advancements in tissue engineering and regenerative medicine have led to the development of various scaffolds designed to support cartilage repair.[3–5]

Hydrogels are three-dimensional (3D) hydrophilic polymer networks capable of water absorption. They mimic the biphasic structure of cartilage, offering a suitable environment for cell growth and matrix formation.[6] Compared to conventional two-dimensional cultures (2D), 3D cell cultivation within hydrogels more accurately replicates *in vivo* conditions, enhancing matrix production. Nevertheless, uneven cell distribution within these gels can hinder uniform matrix formation.[7] 3D bioprinting emerges as a refined technique, precisely controlling biomaterial deposition and cellular placement, and fabricating intricate and biomimetic scaffolds.[8] It can also produce large channels (typically hundreds of micrometers) within the scaffolds. However, the intrinsic pore structure of most hydrogel scaffold materials is often limited to the submicron or nanometer scale, which impedes the acquisition of nutrients and the exchange of metabolic waste in hydrogels, potentially compromising long-term cell viability and tissue functionality.[9]

Porous hydrogels exhibit advantages over their non-porous counterparts in supporting 3D cell culture. However, traditional methods of porosity introduction,[10,11] such as particle leaching, gas foaming, and freeze-drying, involve cytotoxic agents, rendering them unsuitable for live cell encapsulation or integration with 3D printing.[12] The Pluronic micellar template method offers a gentle, all-aqueous approach to hydrogel pore formation, but struggles to create macropores due to micelle size constraints.[13] Consequently, developing a biocompatible, porous bio-ink that supports cell encapsulation remains a formidable challenge. Alternative strategies, like phase separation in emulsions, are hindered by surfactant-induced cytotoxicity, restricting their use in 3D bioprinting.[14,15] The water-in-water system circumvents this issue by segregating two hydrophilic polymer solutions beyond a critical concentration, forming two immiscible aqueous phases without surfactants. The higher volume fraction is used as the continuous phase, and the smaller volume fraction is used as the dispersed phase (water-in-water emulsion).[16] Combining ultraviolet (UV)-curable gelatin precursors with poly(ethylene oxide) (PEO) solutions has yielded porous hydrogels compatible with 3D printing.[17] However, gelatin's inherent mechanical weakness might be exacerbated by internal porosity, limiting its utility in osteochondral engineering. Thus, enhancing hydrogel mechanical stability while retaining porosity is crucial.[18]

Silk fibroin (SF), a natural polymer known for its robust mechanical properties, biocompatibility, degradability, aqueous processability, and functionalizable chemical groups, presents a promising matrix for biomedical scaffolds.[5,19] Silk methacryloyl (SilMA) and methacrylated SF serve as an advanced bio-ink for 3D printing, outperforming methacrylated gelatin in simulating tissues like the heart, blood vessels, trachea, and cartilage. Kim et al.[20] detailed the synthesis of SilMA and its characterization in 3D-printed hydrogel applications for tissue engineering. It was found that a 30% SilMA hydrogel was suitable for cartilage tissue engineering, fulfilling mechanical and biological requirements. Although the high concentration of SilMA enhanced mechanical properties and clinical operability, it also significantly reduced the pore size of the hydrogel (well below 100 μm), which diverges from the ideal pore size for cartilage scaffolds (150–250 μm).[21] This reduction in porosity hinders efficient gas–liquid exchange, adversely affecting the cells loaded in the hydrogel scaffold material through 3D bioprinting. A recent study has explored the fabrication of porous gelatin methacryloyl hydrogels by incorporating PEO. However, this approach also compromised the mechanical properties of the hydrogel.[22]

Recent advances in nanotechnology have integrated nanomaterials into hydrogels to enhance their mechanical properties, broadening their tissue engineering applications. Electrospun NFs are widely used as tissue regeneration scaffolds due to their structure and size resembling collagen fibers in the ECM, as well as their high specific surface area.[23,24] However, the inherent 2D architecture of electrospun membranes substantially limits cellular infiltration into the scaffold interior, compromising their effectiveness in 3D tissue regeneration. This structural limitation has driven recent investigations into developing 3D nanofibrous scaffolds with enhanced cellular interactivity. In our previous study, we developed an innovative 3D SF aerogel by incorporating short electrospun SF NFs into an SF hydrogel matrix, followed by freeze-drying. The resulting nanofibrous aerogel exhibited significantly improved mechanical properties compared to conventional hydrogels. More importantly,

the incorporated nanofibrous architectures substantially enhanced the proliferation and osteogenic differentiation of bone marrow-derived mesenchymal stem cells, suggesting great potential for bone tissue engineering applications.[25]

Therefore, in this study, we developed a 3D printable, NF-reinforced porous SilMA hydrogel designed for cartilage regeneration. PEO was used as a template to increase internal pore structure, and short electrospun SF NFs were incorporated to enhance its mechanical and biological properties. A notable advantage of the water-in-water emulsion system is its inherently low and unstable interfacial tension. The addition of short NFs is expected to improve emulsion stability by reducing the interfacial free energy.[26] Our approach includes characterization of the hydrogel's physicochemical properties, *in vitro* evaluation of biocompatibility and bioactivity, and *in vivo* assessment of chondrogenic ability through subcutaneous implantation in non-obese diabetic/severe combined immunodeficiency mice.

2. Materials and methods

2.1. Materials

Silkworm cocoons were obtained from the Jiangnan Mulberry Silkworm Base (China). Lithium phenyl (2,4,6-trimethylbenzoyl) phosphate (LAP), lithium bromide (LiBr), and hexafluoroisopropanol were obtained from the Shanghai Aladdin Biochemical Technology Co., Ltd. (China), rhodamine-B, PEO, 424 mM glycidyl methacrylate (GMA), and dimethylmethylene blue from Sigma–Aldrich Corporation (United States), Hoechst 33258 and type II collagenase from MedChemExpress LLC (United States), and dialysis bags from Biomedical Instruments Inc (China). Phosphate buffered saline (PBS) was purchased from Thermo Fisher Scientific Inc. (United States), F-12 medium and fetal bovine serum from Gibco (United States), and Live/dead cell staining kit from Shanghai Beyotime Bio-Tech Co., Ltd. (China).

2.2. Extraction of silk fibroin and preparation of nanofibrous film

The silkworm cocoons were first degummed.[27] Then, 10 g of the degummed cocoons were dissolved in a 9.3 mol/L LiBr aqueous solution at 60°C with constant stirring at 300 rpm for 4 h. The resulting solution was dialyzed using a 12–14 kDa dialysis membrane for 4 days to obtain SF. The SF was then dissolved in hexafluoroisopropanol to prepare a 7% (w/w) solution, which was stirred overnight. The solution was then loaded into a 10 mL syringe with an 8-gauge metal needle and connected to electrospinning equipment with the following parameters: a high voltage of 16 kV, a solution flow rate of 15 μL/min, and a distance of 15 cm between the needle and the collector plate. After electrospinning, the NF membrane was placed in a fume hood overnight, followed by cross-linking with absolute ethanol for 15 min and drying at room temperature.[28] The electrospun NFs were subsequently weighed and homogenized in deionized water to obtain a suspension of short NFs, which was stored at 4°C for further use.

2.3. Synthesis of silk methacryloyl

Briefly, degummed silk was dissolved in LiBr and reacted at 60°C for an hour under constant stirring at 300 rpm. GMA (424 mM) was then added to the solution, and the mixture was stirred for an additional 3 h for the functionalization reaction between SF and GMA. The reaction mixture was transferred to a dialysis membrane (molecular weight cut-off: 12,000–14,000) and dialyzed against deionized water for 4 days. Finally, the dialyzed solution was freeze-dried to obtain SilMA for future use.[20]

2.4. Preparation of silk methacryloyl hydrogels with poly(ethylene oxide)-induced porosity and nanofiber reinforcement

The prepared silk NF membrane samples were homogenized to form short NF suspensions. SilMA powder, LAP powder (Aladdin, China), and the NF suspensions were thoroughly mixed and dissolved in the culture medium to prepare a final solution with concentrations of 30% w/v for SilMA, 0.25% w/v for LAP, and 1 and 2% w/v for NFs. This composite solution was used as the non-porous hydrogel precursor solution. PEO (molecular weight = 300,000) powder was dissolved separately in the culture medium to prepare a 1.6% w/v solution. The hydrogel precursor and PEO solutions were then mixed at a volume ratio of 2:1 to form a two-phase aqueous emulsion, which served as the porous hydrogel precursor solution. The porous hydrogel was prepared using UV light-induced cross-linking, followed by PEO precipitation through immersion. Regarding 3D bioprinting, the hydrogel structures were fabricated using a digital light processing (DLP) 3D bioprinter (ZJ-BP01, Zhongjian 3D Technology Co., China) equipped with a 405 nm UV light source (intensity: 20 mW/cm^2). The printer was integrated with a temperature-controlled vat (maintained at 4°C) to prevent premature gelation of the photopolymerizable hydrogel precursor. The detailed 3D printing parameters are shown in Table 1.

2.5. Characterization

2.5.1. Proton nuclear magnetic resonance and Fourier transform infrared spectroscopy

SF and SilMA were weighed and dissolved in 0.5 mL of deuterated dimethyl sulfoxide. The resulting solutions were transferred to a nuclear magnetic resonance (NMR) tube to determine proton NMR (1H-NMR). For Fourier Transform infrared spectroscopy (FTIR), SF, SilMA,

Table 1. Three-dimensional printing parameters

Project	Parameter
Digital model	
Low-temperature cylinder	Cell-laden poly(ethylene oxide)/ nanofiber/silk methacryloyl bio-ink
Print parameter	
Printing model	Lattice shape
Cube dimension	6.6 × 7.8 × 3.0 mm
Pattern filing	Cross-mesh
Strand spacing	0.6 mm
Layer height	0.6 μm
Number of layers	4
Temperature	25.0°C
Print parameter	
Layer thickness	0.02 mm
Base layer count	5
Base exposure time	30 s
Exposure time	8 s
Transition layer count	0
Transition type	Linear
Transition layer delay	0 s
Base lifting delay (before)	2 s
Base lifting delay (after)	0.5 s
Base retract delay	2 s
Lifting delay (before)	2 s
Cross-linking	Blue light (405 nm, 20 mW/cm^2)
Print platform	
Resolution	X:1920 pixels and Y: 1080 pixels

SilMA hydrogels, and soaked PEO/SilMA hydrogels were lyophilized and ground into powder. Each sample was mixed with a small amount of finely ground LiBr and exposed to infrared light for FTIR detection.

2.5.2 Morphology and porosity

A scanning electron microscope (SEM) (Model: GeminiSEM 300, ZEISS, Germany) was used to observe the internal structure of each group of hydrogels and the distribution of NFs (15 kV accelerating voltage). The SEM images were statistically analyzed using ImageJ software (version 1.51j8) for pore size and porosity of each group of hydrogel structures with and without microporous structures (n = 3). The pore size structures and PEO emulsion droplets in the hydrogels were directly observed using optical microscopy (DM6 B, Leica, Germany). The hydrogels were labeled with rhodamine-B, followed by hematoxylin and eosin (HE) staining. The microporous structures of the hydrogels were then observed with an orthostatic microscope (DM6 B, Leica, Germany).

2.5.2. Swelling properties

Hydrogel samples (diameter = 10 mm, height = 3 mm) were prepared, and their initial weights were recorded as M0. Each group of hydrogel samples was transferred into a 12-well plate, and 3 mL of PBS solution was added to each well. The plate was placed in a constant-temperature incubator at 37°C. The samples were removed at the predetermined time points (1, 3, 6, 9, 12, and 24 h), and excess surface moisture was quickly absorbed using highly absorbent filter paper. The samples were photographed, and the observations were recorded. The samples were weighed again, and the weights were recorded as M1. The swelling ratio of the hydrogel was calculated using the following formula in **Equation I**:

$$(M1-M0) / M0 \times 100\% \quad (I)$$

2.5.3. Mechanical test

The mechanical properties of each group of hydrogels were measured using a universal material compression machine (RIGOL, China). Cylindrical samples (diameter = 10 mm, height = 6 mm), prepared using silicon molds, and 3D-printed grid-like samples (described in **Section 2.4**) were subjected to uniaxial compression testing at a rate of 5 mm/min. Stress–strain curves/elastic modulus were obtained (n = 3). The compressive modulus was calculated as the slope of the linear elastic region within the 20–40% strain interval of the stress–strain curve. To evaluate the fatigue resistance of the 3D-printed scaffolds, cyclic compressive loading-unloading tests were conducted under 50% strain for 500 consecutive cycles at a rate of 5 mm/min, without intermittent recovery periods.

2.5.4. Rheological measurements

The light-curing properties of the gel precursors were evaluated through rheological analysis. Dynamic rheological experiments were conducted using a rotational rheometer (Anton Paar, Austria) equipped with a 25 mm measuring rotor to assess the rheological properties of the PEO/NF/SilMA composite hydrogels at 25°C. The gel point test was performed in time–scan oscillation mode under 10% strain, 1 Hz frequency, and a 0.5 mm gap, with UV illumination for 100 s. The gel point was determined as the intersection of the curves where the storage modulus (G′) surpassed the loss modulus (G″). For the amplitude scan, the G′ and G″ were measured by maintaining a constant frequency at 10 rad/s and varying strain values from 0.01 to 1%. For the frequency scan, G′ and G″ were measured

by keeping the shear strain constant at 1% and varying the frequency range from 0.158 to 25.1 rad/s.

2.6. Isolation and cultivation of rat articulator chondrocytes

The cartilage from the knee joints of 24-h old male Sprague Dawley rats (n = 4) (Laboratory Animal Center of Anhui Medical University (Hefei, Anhui Province, China) was extracted under sterile conditions. The cartilage slices were washed with PBS and then digested with 0.25% trypsin (BioFroxx, Germany) for 30 min, followed by three additional PBS washes. Subsequently, the slices were digested with 0.3% type II collagenase (MCE, United States) at 37°C for 4 h. The digested solution was filtered through a 70 μm cell strainer (BioSharp, China) to remove collagen impurities and then centrifuged at 1000 rpm for 5 min to collect articulator chondrocytes (ACs). The cells were cultured and expanded in Dulbecco's Modified Eagle Medium/F-12 complete medium at 37°C, 95% humidity, and 5% carbon dioxide. ACs from passages 2–3 were used for experiments. For the cell-laden 3D printing, the ACs were mixed into the bio-ink before printing. The cell-loaded hydrogels were immersed in a culture medium immediately following the 3D printing process.

2.7 *In vitro* cytocompatibility and cartilage formation

2.7.1. Live/dead cell staining

Hydrogels loaded with ACs (1×10^6 cells/mL) were prepared and incubated for 1 and 7 days to evaluate cell viability. Cell viability was assessed using a live/dead staining kit (Beyotime, China). The staining solution was prepared by diluting the dyes to a final concentration of 2.5 μM calcein acetoxymethyl ester and 1.25 μM propidium iodide. The AC-laden hydrogels were immersed in 400 μL of the diluted staining solution and incubated at 37°C for 30 min in the dark. The growth of ACs within the hydrogels was observed using a confocal microscope (ZEISS, Germany).

2.7.2. Quantification of DNA and glycosaminoglycan

For the quantitative measurement of DNA and glycosaminoglycan (GAG) content in hydrogels, AC-laden hydrogel samples were incubated for 7 and 14 days in Eppendorf tubes containing 1 mL of PBS, followed by homogenization using a homogenizer. Then, 2 μL of proteinase K solution (Ron, China) was added to the homogenized solution, and the mixture was incubated in a water bath at 56°C for 6 h. After centrifugation, the supernatant was collected. DNA content was determined using Hoechst 33258 dye (MCE, United States). The fluorescence intensity of each sample was measured using a microplate reader (PerkinElmer, United States) at an excitation wavelength of 360 nm and an emission wavelength of 460 nm. GAG content in the supernatant was quantified using the dimethylmethylene blue colorimetric method (n = 3).

2.7.3. Histological analyses

To assess the viability and distribution of ACs within the hydrogel during *in vitro* culture, hydrogel samples containing cells were cultured for 21 days. The samples were then fixed with 4% paraformaldehyde, embedded in paraffin, and sectioned at 5 μm. Sections were stained with HE, Safranin O, and Alcian Blue to evaluate the survival of ACs after 21 days of culture.

2.7.4. Real-time quantitative polymerase chain reaction

The expression levels of MKI67, collagen II (*COL2A1*), aggrecan (*ACAN*), and SRY-box transcription factor 9 (*SOX9*) genes in ACs were evaluated using real-time quantitative polymerase chain reaction (RT-qPCR) across different hydrogel groups. Total RNA was isolated from the cells using Trizol reagent, followed by reverse transcription to synthesize complementary DNA. RT-qPCR was conducted using TB Green Premix Ex Taq™ II FAST qPCR kit (Takara Bio, United States). Data was analyzed using the $2^{-\Delta\Delta CT}$ method to determine means and standard deviations. The primer sequences utilized in this study are detailed in Table S1. This experiment was repeated thrice, with each group having three replicate wells per repetition.

2.8. Formation of *in vivo* cartilage

2.8.1. Subcutaneous implantation of articulator chondrocyte-laden hydrogels in non-obese diabetic/severe combined immunodeficiency mice

Animal experiments were approved by the Animal Welfare Ethics Committee of the Anhui Provincial Center for Disease Control and Prevention (No.: 2024024). Porous and non-porous hydrogel precursors were prepared as described previously. ACs were mixed into the prepared hydrogel precursors at a concentration of 1×10^8 cells/mL, serving as the bio-ink. The bioprinting parameters are detailed in Table 1. During the bioprinting process, the photocrosslinkable bio-ink was cured under continuous UV light irradiation. After bioprinting, the cell-laden constructs were cultured in a complete medium for 7 days and then transplanted into both sides of the back of male non-obese diabetic/severe combined immunodeficiency mice (n = 4) to observe *in vivo* cartilage formation.

2.8.2. Histological and immunohistochemical staining

The specimens were collected and subjected to histological and immunohistochemical analyses. Briefly, the samples were fixed with 4% paraformaldehyde, embedded in

paraffin, and sectioned at 5 μm. The sections were stained with HE, Safranin O, and Alcian Blue, and immunohistochemically stained for collagen II (Col-II) and collagen I (Col-I). The positive area and average optical density values of Col-II and Col-I were statistically analyzed through Image J software (version 1.51j8).

2.9. Statistical analysis

All data were expressed as mean ± standard deviation. The data were analyzed using one-way analysis of variance with GraphPad Prism version 9.5.1, and $p < 0.05$ was considered statistically significant.

3. Results and discussion

3.1. Preparation of silk methacryloyl hydrogels and electrospun silk fibroin nanofibers

Figure 1A displays the ^{1}H-NMR spectra of the prepared SF and SilMA. Notably, the presence of vinyl methacrylate signals at δ = 6.2–6.0 parts per million (ppm) and δ = 5.8–5.6 ppm in the spectrum of SilMA, along with the methyl group signal at δ = 1.8 ppm and a gradual decrease in the lysine methylene signal at δ = 2.9 ppm, suggests that the lysine residues in SF underwent chemical modification. Additionally, a detectable signal at δ = 3.2–3.6 ppm was observed, which is attributed to hydrogen in the adjacent carbon–nitrogen bond. In the FTIR spectrum of SF, the characteristic β-sheet amide I, amide II, and amide III bands were identified. For SilMA, in addition to these β-sheet features, a weak absorption band at 1297 cm^{-1} was observed, corresponding to the CHOH group stretching from the alcohol group in GMA following the epoxy ring opening. Furthermore, a change at 1118 cm^{-1} was also detected, corresponding to methylene rocking vibrations of the vinyl methacrylate group in GMA (Figure 1B).[20] Collectively, FTIR and ^{1}H-NMR spectra demonstrated the successful extraction and methacrylation of SF. As demonstrated in Figure S1A, the SilMA solution containing LAP transitioned from a liquid to an immobile gel state under UV irradiation. Additionally, SEM images (Figure S1B) revealed that the electrospun SF NFs exhibited uniform, smooth morphology, and nanoscale diameters, confirming successful SF NF fabrication.

3.2. Preparation of nanofiber-enhanced porous silk methacryloyl hydrogels

The water-in-water emulsion principle, describing the phase separation that occurs when two hydrophilic polymer solutions are mixed under specific conditions, was applied in this study to create pores in the hydrogel. This phenomenon requires polymer concentrations to exceed a critical threshold (1.6% w/v for PEO was chosen based on previous studies), disrupting thermodynamic equilibrium and forming immiscible aqueous phases.[29] As shown in Figure 1C, both SilMA and PEO/SilMA groups exhibited acceptable 3D printing performances. The PEO/SilMA combination yielded translucent matte-white hydrogels, while NFs-incorporated groups exhibited opaque white coloration with significantly enhanced printability, consistent with previous findings.[30–32] While nanomaterials enhanced hydrogel formability and mechanical strength in 3D bioprinting, it was noticeable that excessive nanomaterial concentrations might compromise mechanical reinforcement. The sample with 3% NFs could not be formed during the 3D printing in this study. Regarding the concentration of PEO, initial trials using a 1:1 volumetric ratio of 2%NF/SilMA and PEO emulsion produced unprintable hydrogels (Figure S2). Therefore, a revised 2:1 mixing ratio was selected. To evaluate potential PEO residue in hydrogels after immersion-induced precipitation, SilMA and PEO/SilMA hydrogels soaked for 2 days were lyophilized and analyzed using FTIR spectroscopy (Figure 1B). The near-identical FTIR spectra of both hydrogel groups confirmed complete PEO removal after the 2-day immersion. This outcome establishes a biocompatible foundation for cell-laden hydrogel fabrication using PEO-based assembly.

3.3. Characterization of nanofiber-enhanced porous silk methacryloyl hydrogels

3.3.1. Morphology and porosity

Figure 2A schematically illustrates the internal structures of SilMA, PEO/SilMA, and PEO/NF/SilMA hydrogels. Optical microscopy revealed PEO emulsion droplets within the matrix to characterize the NF-enhanced porous hydrogels. Due to the reduced light transmittance in hydrogels after NF incorporation, SilMA, and PEO/SilMA hydrogels were selected for structural observation. As shown in Figure 2B, the SilMA group contained small droplets formed through self-cross-linking, while the PEO/SilMA group exhibited significantly larger near-spherical PEO emulsion droplets, confirming the pore-forming effect of PEO phase separation. The hydrogel microstructure was characterized using SEM, rhodamine B staining, and HE staining (Figure 2C). SEM images revealed a well-defined porous architecture in the PEO-incorporated groups, while only cross-linking-induced micropores were observed in non-porous counterparts. Although NFs were detectable as nanofillers, their incorporation did not compromise the microporous structure of SilMA hydrogels. In NF-containing groups, NFs were primarily localized within the hydrogel matrix and on pore walls, resulting in an increased surface roughness compared to NF-free samples. Notably, the 1%NF/SilMA and 2%NF/SilMA groups exhibited limited NF dispersion areas with visible aggregation and surface pits. With the introduction

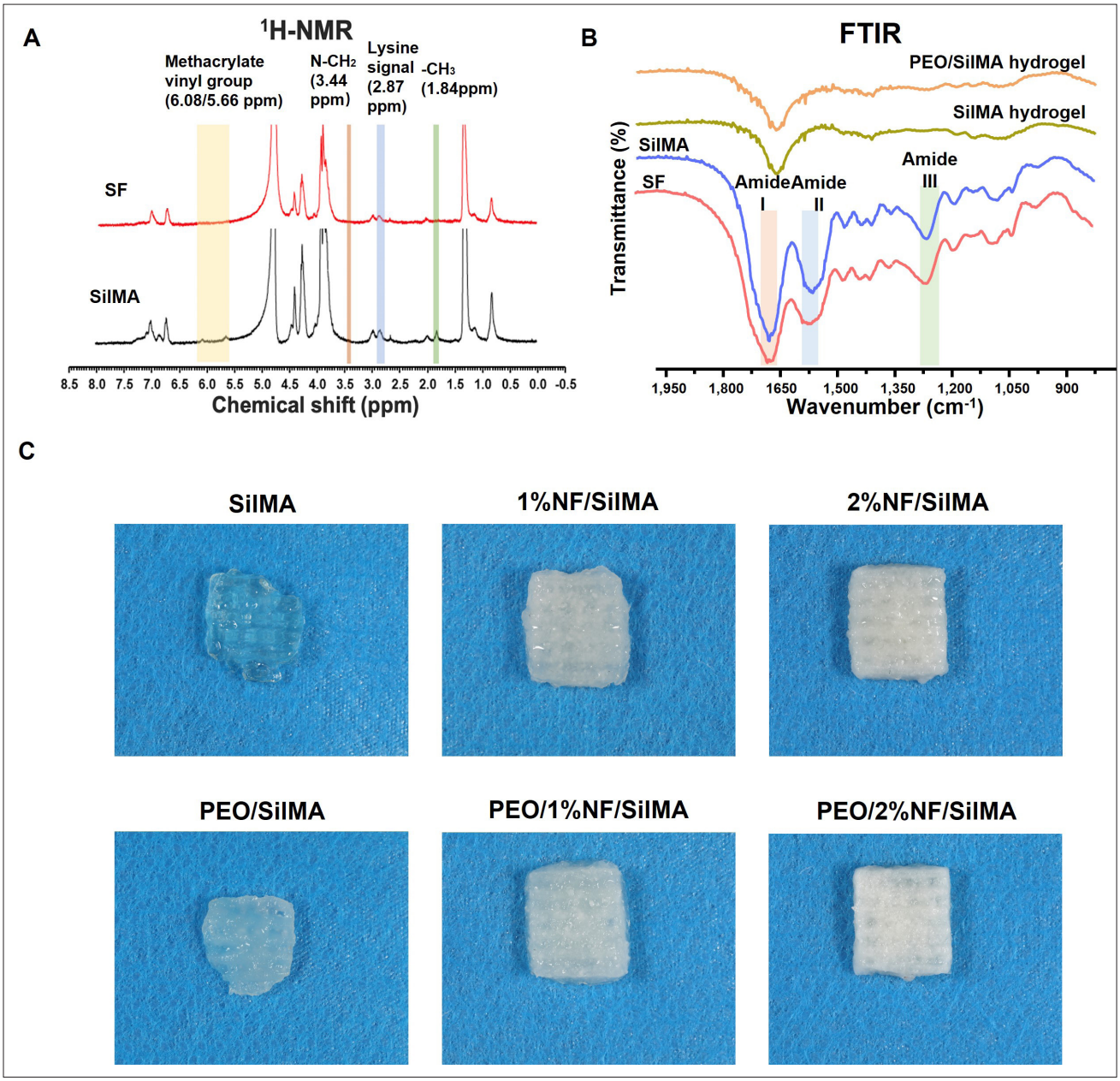

Figure 1. Preparation and characterization of SilMA-based hydrogels with NF-enhanced mechanics and PEO-induced porosity. (A) The 1H-NMR spectra of SF and SilMA. (B) FTIR spectra of SF, SilMA, freeze-dried SilMA hydrogels, and PEO/SilMA hydrogels after 2-day immersion in deionized water. (C) Photographs of three-dimensional-printed hydrogel scaffolds of SilMA, 1%NF/SilMA, 2%NF/SilMA, PEO/SilMA, PEO/1%NF/SilMA, and PEO/2%NF/SilMA. Abbreviations: 1H-NMR, proton nuclear magnetic resonance; FTIR, Fourier transform infrared spectroscopy; NF, nanofibers; PEO, poly(ethylene oxide); SEM, scanning electron microscopy; SF, silk fibroin; SilMA, silk methacryloyl.

of PEO, PEO/1%NF/SilMA and PEO/2%NF/SilMA groups showed improved NFs distribution uniformity compared to 1%NF/SilMA and 2%NF/SilMA groups. The PEO/1%NF/SilMA group achieved optimal NF dispersion within the hydrogel matrix and along pore walls, whereas minor NF aggregation persisted in the PEO/2%NF/SilMA group. This phenomenon might be due to the higher NF concentration per interfacial area exceeding optimal dispersion capacity,[33] whereas the 1% formulation maintains favorable spatial distribution under equivalent geometric constraints. Rhodamine B staining was achieved by conjugating the dye with the SilMA cross-linking network, enabling red fluorescence emission from the hydrogel matrix while the pores appeared dark. The

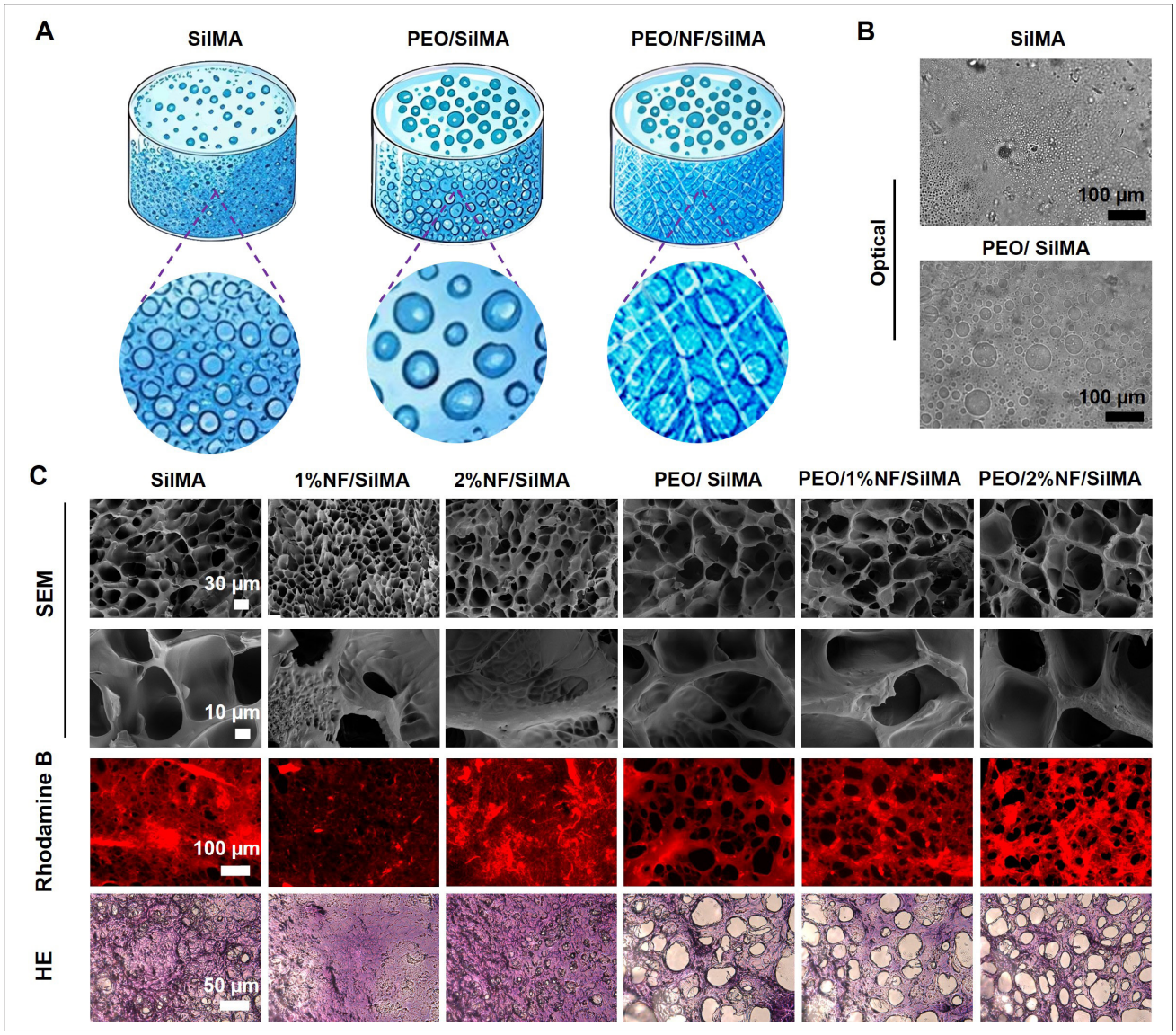

Figure 2. Morphology and porosity. (A) The schematic diagram illustrates the internal porosity of SilMA, PEO/SilMA, and PEO/NF/SilMA hydrogels. (B) Optical microscope images of SilMA and PEO/SilMA hydrogels. Scale bar: 100 μm; magnification: 10×. (C) SEM image, rhodamine-B staining (the hydrogel network coupled with rhodamine shows red fluorescence, and the pore structure shows a dark area), and HE staining images of the six groups of hydrogels. Scale bars: 10, 30, 50, and 100 μm; magnification: 1000×, 300×, 200×, 100×. Abbreviations: HE, hematoxylin and eosin; NF, nanofibers; PEO, poly(ethylene oxide); SEM, scanning electron microscopy; SilMA, silk methacryloyl.

results revealed significantly increased pore quantity and size in porous groups. NFs were observed as filamentous structures within the hydrogel matrix. HE staining further confirmed PEO-derived pores.

Quantitative analysis of pore size distribution and porosity was performed using ImageJ software on SEM images of six hydrogel groups (Figure 3A–F). The histograms demonstrated more centralized pore distributions in PEO/1%NF/SilMA and PEO/2%NF/SilMA compared to PEO/SilMA. This phenomenon suggests that incorporating short NFs may enhance emulsion droplet stability by reducing interfacial free energy at the phase boundaries.[34] SilMA had an average pore diameter of 20.07 ± 4.67 μm, consistent with previous literature,[20] while 1%NF/SilMA and 2%NF/SilMA groups exhibited average pore diameters of 17.25 ± 3.59 μm and 16.25 ± 3.59 μm, respectively. Incorporating NFs reduced the pore size of SilMA hydrogels, though no significant difference was observed between 1%NF/SilMA and

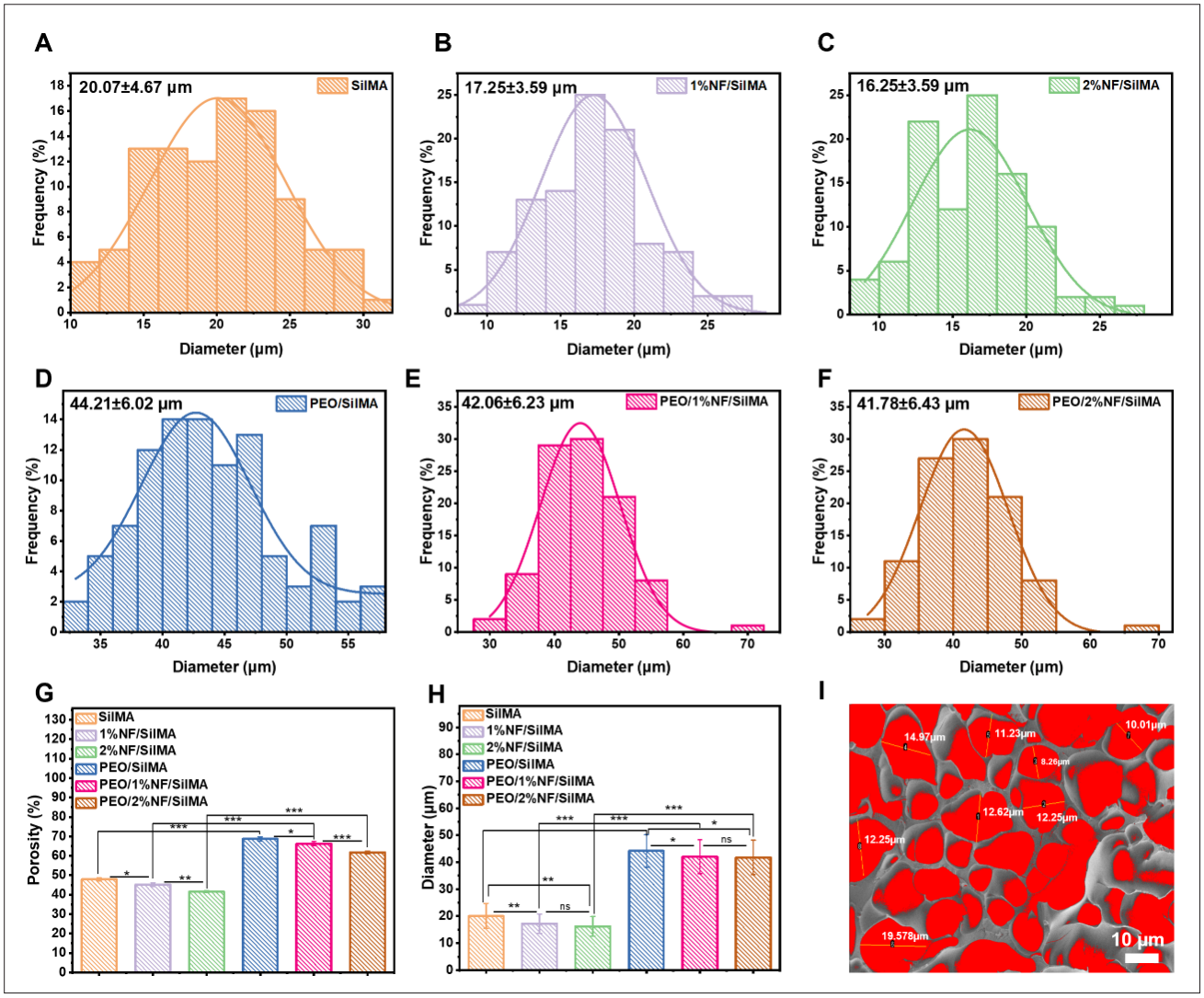

Figure 3. Quantitative analysis of pore distribution and pore size. (A–F) Pore diameter distribution in each group of samples, statistical analysis of 100 pores randomly selected from each group. (G) Average aperture statistics. (H) Porosity statistics. (I) Statistical method of pore diameter and pore area. Scale bar: 100 μm; magnification: 1000×. *Note*: Statistical significance at $*p < 0.05$, $**p < 0.01$, $***p < 0.001$. Abbreviations: NF, nanofibers; ns, non-significant; PEO, poly(ethylene oxide); SilMA, silk methacryloyl.

2%NF/SilMA. For PEO-incorporated groups, the average pore diameters increased to 44.2 ± 6.02 μm, 42.06 ± 6.23 μm, and 41.78 ± 6.23 μm for PEO/SilMA, PEO/1%NF/SilMA, and PEO/2%NF/SilMA, respectively, representing an approximate two-fold enlargement compared to non-porous counterparts. The statistical analysis of pore size and porosity of different groups of hydrogels is displayed in Figure 3G and H. It can be seen that incorporating PEO not only significantly increased the pore size in the samples but also enhanced their porosity (by approximately 50%). Previous articles have reported that a scaffold porosity of around 70% is required for sufficient cell infiltration and regeneration.[35,36] The porosity ranges between 60 and 70% in the groups with pores induced by PEO. This implies that PEO was highly necessary for the pore formation of 3D-printed SilMA hydrogel in this study. The increase in pore size and porosity of the hydrogel will facilitate the exchange of nutrients and oxygen for chondrocytes within the gel.[37,38]

However, the most suitable scaffold pore size for cartilage regeneration is approximately 150–250 μm.[21,39,40] Herein, 3D printing technology was adopted to create a microporous structure in the hydrogel, resulting in a dual-level structure that combines macropores and micropores. This structure is advantageous for promoting

cell proliferation, chondrogenesis, and angiogenesis. As shown in Figure S3, the spacing between the two strands of the PEO/SilMA group scaffold (612.6 ± 32.8 μm) closely matched the strand spacing and layer height set for 3D printing (600 μm). However, with the addition of NFs, the distance between the strands decreased. When 2% NF was added, the spacing between the strands was reduced to approximately 400 μm (378.9 ± 89.2 μm). This phenomenon may be due to: (i) the relatively large length of the NFs, causing the fibers located at the edges of the strands to be fixed at the mesh edges after the hydrogel was photocured, or (ii) the introduction of NFs led to a decrease in the fluidity of the printing bio-ink, reducing the printing accuracy. Although this large pore size did not reach the size recommended in the literature (about 200 μm),[41] a previous study has reported that scaffolds with a pore size of 400 μm could promote proteoglycan production and chondrogenic marker gene expression more effectively than those with smaller pore sizes of 200 and 100 μm.[42] While smaller macropores could be achieved by setting a smaller strand spacing or layer height to 400 μm before 3D printing, the possible unevenness or aggregation of NFs during preparation could reduce printing reproducibility. Therefore, a strand spacing of 600 μm was chosen for 3D printing in this study.

3.3.2. Swelling and mechanical properties

The swelling behavior of hydrogels was systematically evaluated to assess their hydrophilicity and structural stability—two critical determinants for nutrient diffusion and long-term functionality in cartilage regeneration. Macroscopic observation (Figure S4) revealed significant volumetric expansion in PEO-modified groups, with pore architectures maintained throughout the 24-h PBS immersion, contrasting with the non-porous controls. Quantitative swelling kinetics (Figure 4A) demonstrated a biphasic absorption pattern: rapid initial swelling (0–12 h, >80% equilibrium absorption) followed by gradual stabilization. Notably, PEO/SilMA and PEO/1%NF/SilMA groups exhibited prolonged swelling phases, achieving equilibrium swelling ratios of 170.1 ± 7.50% and 162.7 ± 2.76% at 24 h, respectively. This delayed equilibration might be attributed to the hierarchical pore structure (relative macroporosity from PEO leaching combined with inherent SilMA microporosity), which creates capillary-driven fluid transport pathways distinct from conventional homogeneous networks. Compared to a previous study that reported the swelling rate of only 6% for nanosilicate-reinforced SF hydrogel, measured using the same method,[43] the NF/SilMA/PEO hydrogels in this study had outstanding swelling behavior.

The regenerative capacity of the scaffold also fundamentally depends on its mechanical properties. These properties must be robust enough to withstand articulation and handling during implantation. Additionally, they should not be overly strong to the extent that they cause stress shielding of mechanosensitive cells.[44] In this study, to investigate the differences in the mechanical properties between grid-like hydrogels with macroporous structures fabricated via 3D printing and those without macropores, we also prepared cylindrical samples using molds and subjected them to compression testing. Figure 4B and C shows the compression test results of the cylindrical samples, while Figure 4D and E displays the mechanical properties of the 3D-printed grid-like samples. In general, the compressive strength of cylindrical samples was slightly higher than that of the corresponding 3D-printed samples. The compressive strength of the cylindrical SilMA hydrogels reached 1235.8 ± 172.1 kPa, while the strength of the grid-like samples was only 930.2 ± 85.6 kPa. Although the latter is slightly lower, this value was also close to the compressive strength of 3D-printed 30% SilMA hydrogel reported in previous studies.[20] Regarding the compressive modulus, the grid-like samples in each group exhibited better performance compared to the cylindrical samples. It is speculated that the cylindrical samples could transfer and disperse stress better, reducing local stress concentration and resulting in higher compressive strength. In the grid structure, stress tends to concentrate at the nodes, leading to earlier material failure. The reason for the larger compressive modulus of the grid structure could be attributed to the better force dispersion by the truss structure, causing less deformation of the scaffold. Notably, using PEO in the preparation of SilMA hydrogel significantly reduced its compressive strength and modulus. However, the addition of NFs could reverse this negative influence. The PEO/2%NF/SilMA group possessed similar mechanical properties to the SilMA group for both cylinder shape and grid-like structure. Specifically, the compressive modulus of the 3D-printed PEO/2%NF/SilMA (815.0 ± 73.1 kPa) had reached that of native cartilage (around 0.81 ± 0.56 MPa),[45] indicating the promising potential for cartilage repair applications. In addition, the strength of the hydrogel is not invariably augmented with an increase in the concentration of NFs. The 2%NF/SilMA exhibited obvious mechanical deterioration compared to SilMA and 1%NF/SilMA. This aligns with previous reports suggesting that excessive nanomaterial concentrations may compromise mechanical reinforcement.[32,33] This could also be explained by the percolation theory predictions—excessive NF loading induces aggregation, creating stress concentration points rather than continuous reinforcing networks. However, the 3D-printed PEO/2%NF/SilMA groups showed better mechanical properties than the

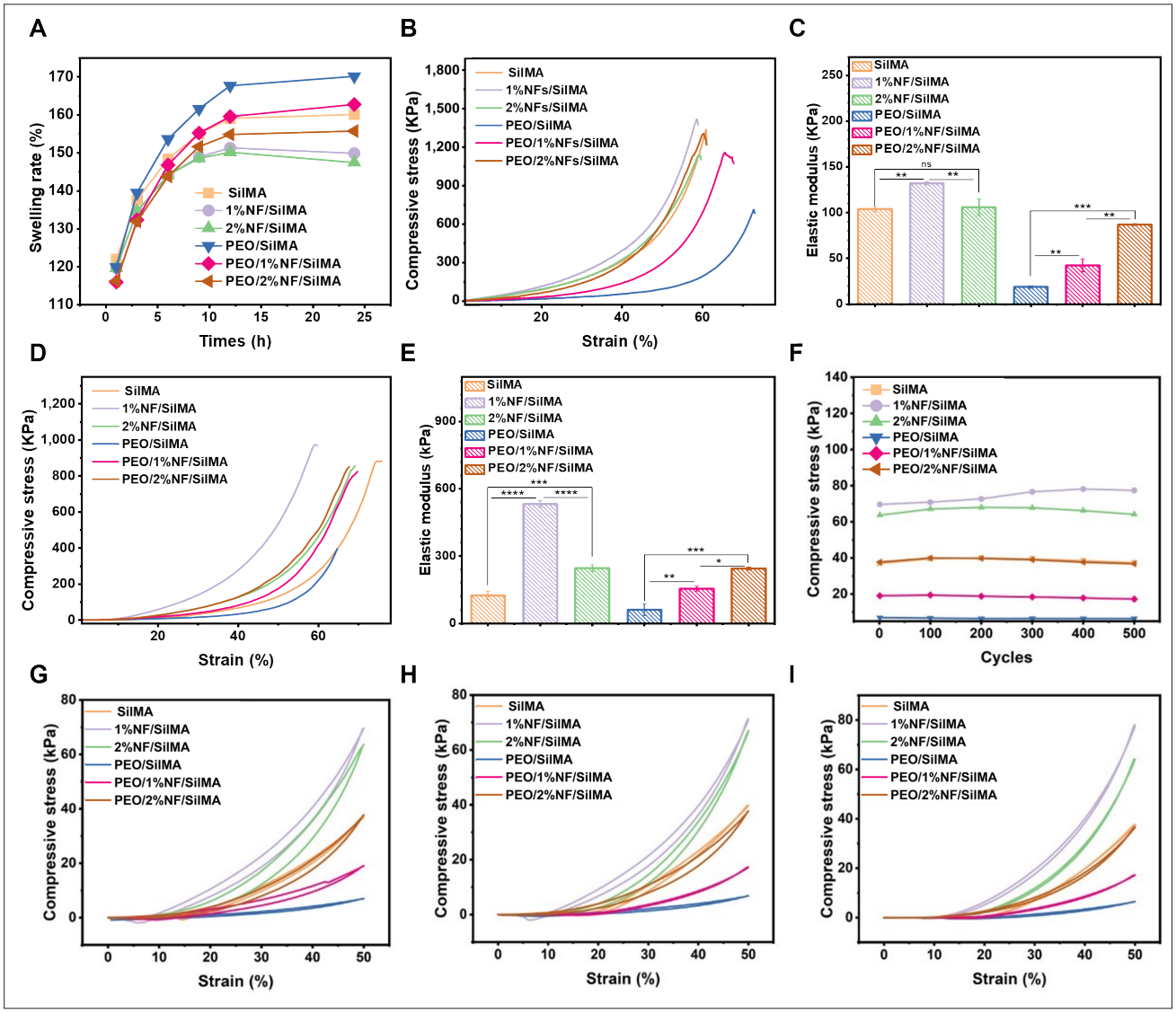

Figure 4. Swelling performance and mechanical properties. (A) Swelling kinetic profiles at different time points (1, 3, 6, 9, 12, and 24-h). (B and C) Stress–strain diagram and compression modulus of different cylindrical groups. (D and E) Stress–strain diagram and compression modulus of different three-dimensional-printed groups. (F) Compressive strength of each 3D-printed group at different cycles during the cyclic compressive loading testing. Stress–strain curves of each group at the (G) 1st, (H) 100th, and (I) 500th cycle, respectively. *Note*: Statistical significance at $^{*}p < 0.05$, $^{**}p < 0.01$, $^{***}p < 0.001$. Abbreviations: NF, nanofibers; PEO, poly(ethylene oxide); SilMA, silk methacryloyl .

3D-printed PEO/1%NF/SilMA groups. This result might be due to the reduction of uneven fiber aggregation caused by a relatively high concentration of NFs during the PEO-induced pore formation process.

As previous studies have shown, NFs, as gel fillers, could effectively enhance their fatigue resistance properties,[24] which is also crucial for cartilage scaffold materials that are subjected to stress. The results of cyclic compressive loading-unloading tests performed on 3D-printed grid-like samples (Figure 4F–I) demonstrated the positive effect of the introduction of NFs to the prepared hydrogels. The compressive strength of the hydrogels in each group did not significantly decrease after 500 compression cycles (Figure 4F), and they showed the same trend between groups (Figure 4D). In addition, by comparing the cyclic compression curves of the 1st, 100th, and 500th compression (Figure 4G–I), it can be observed that the area of the hysteresis loop of the hydrogel scaffolds in each group became smaller and more stable after repeated cyclic compressions. Figure S5 specifically shows the stress–strain curves of each group within 500 cycles of compression,

which further suggests that as the number of compressions increased, the structures, such as the polymer chains and cross-linking networks inside the hydrogel scaffolds, gradually became stable with reduced energy dissipation. It indicates that the material had a certain degree of self-adaptability and stability. When subjected to repeated loads, it was able to ensure that the mechanical properties were maintained and energy consumption was reduced, making it suitable for cartilage repair scenarios that involve bearing dynamic loads.

3.3.3. Rheological performance

The viscoelastic properties of hydrogels were rigorously characterized through oscillatory rheometry, providing critical insights into their structural integrity under dynamic loading. Strain sweep tests (Figure 5A–F) revealed that the storage modulus (G′) exceeded the loss modulus (G″) within the strain range of 0.01–1%, indicating solid-like behavior. The G′ and G″ curves of 1%NF/SilMA, PEO/1%NF/SilMA, and PEO/2%NF/SilMA remained parallel in this range, suggesting enhanced structural stability due to NF incorporation. However, the 2%NF/SilMA group exhibited a declining trend near 1% strain, indicating partial structural disruption. Frequency sweep tests (Figure 5G–K) showed minimal stress changes at low frequencies and significant changes at high frequencies. The increase in G′ for 1%NF/SilMA, PEO/1%NF/SilMA, and PEO/2%NF/SilMA groups confirmed improved hardness and stability with NFs. Conversely, the decrease in G′ for the 2%NF/SilMA indicated mechanical degradation. The rise in G″ in NF-containing groups suggested weak interfacial bonding between NFs and the hydrogel matrix, as well as suboptimal cross-linking, consistent with mechanical performance results.[20]

The UV-curable hydrogel underwent a rapid formation of its structural network within seconds under UV light, which was effectively monitored and characterized using rheological methods. A transition from G" > G' to G' > G" was observed, indicating a shift from viscosity-dominated to elasticity-dominated behavior in the hydrogel (Figures 5K and S6). The gelation times for different groups were summarized based on the crossover points in the local plots (Figure 5L). Notably, the gelation times of 1%NF/SilMA and 2%NF/SilMA groups showed no significant difference compared to the SilMA group, which suggested that the 30% SilMA hydrogel inherently possesses a densely crosslinked network, and the addition of NFs does not accelerate the gelation process. Jin et al.[46] have reported that excessive incorporation of nanomaterials may disrupt the curing system of hydrogels.[33,46] In the case of PEO/SilMA hydrogels, the extended gelation time is likely due to the dispersed cross-linking network caused by the presence of PEO emulsion.

3.4. *In vitro* study of cytocompatibility and cartilage tissue engineering

3.4.1. Live/dead cell staining

Compared to conventional 2D cell culture systems, 3D culture better replicates physiological microenvironments. Scaffold materials must simultaneously support long-term cell survival and actively promote cartilage regeneration.[47,48] We evaluated AC performance in hydrogels through viability and proliferation assays. Cell-laden hydrogels were cultured for 1 and 7 days, with viability assessed via live/dead staining. On Day 1, all groups showed sparse viable ACs (green fluorescence) with minimal dead cells (red fluorescence) (Figure 6A). Prolonged culture revealed significant cell population growth, confirming hydrogel biocompatibility for extended cultivation. The hydrogels with pores formed by PEO demonstrated higher AC density than the regular controls, indicating that PEO incorporation significantly enhanced proliferation, aligning with established literature.

3.4.2. DNA content and glycosaminoglycan deposition

The proliferation of ACs within the hydrogel scaffolds was further quantified through DNA quantification after 7- and 14-day cultures (Figure 6B). While all groups showed time-dependent increases, PEO-modified hydrogels consistently exhibited higher DNA content than their non-porous counterparts at both time points. These findings confirm that hydrogels with larger pore size and porosity produced by PEO create superior 3D microenvironments for AC proliferation.[22] GAG deposition serves as a key indicator of chondrocyte functionality.[49] Therefore, GAG secretion of AC in hydrogels was further measured (Figure 6C). Given that initial cell seeding density influences GAG quantification, we normalized GAG values to DNA content to eliminate inter-sample variability (Figure 6D). On Day 7, it can be seen that incorporating PEO enhanced cell proliferation and GAG production but adding NFs had no noticeable effect. This trend, induced by PEO modification, was intensified with prolonged culture on Day 14. At that time, the introduction of NFs also exhibited a significant positive effect on GAG deposition, especially for the 1% concentration. The enhanced performance of porous hydrogels might be attributed to PEO-induced porosity, which facilitates oxygen and nutrient transport.[50] Additionally, the exceptional GAG deposition observed in the PEO/1%NF/SilMA group could be attributed to the homogeneous distribution of NFs and larger pores within the hydrogel matrix, which modulated ACs' behavior at the microscale.

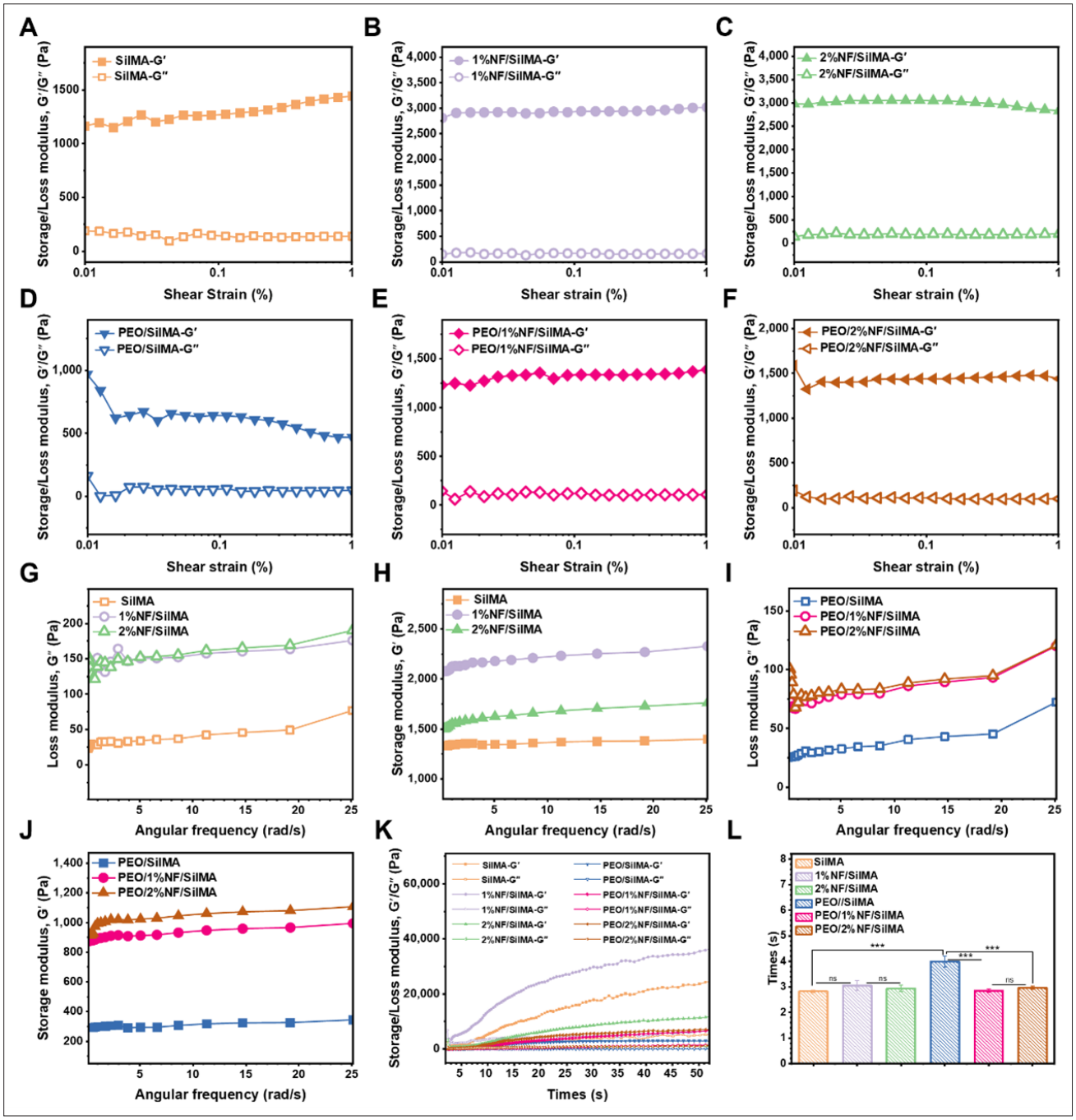

Figure 5. Rheological analysis of hydrogels. (A–F) The loss modulus (G") and storage mode (G') of each group of hydrogels depend on the change of amplitude scanning. (G–J) The G" and storage mode G' of each group depend on the change of frequency scanning. (K) UV time oscillation scan to observe the G" and storage mode G'. (L) The gel time point of each group of hydrogels according to the UV time oscillation scan. *Note*: Statistical significance at $^{*}p < 0.05$, $^{**}p < 0.01$, $^{***}p < 0.001$. Abbreviations: NF, nanofibers; ns, non-significant; PEO, poly(ethylene oxide); SilMA, silk methacryloyl; UV, ultraviolet.

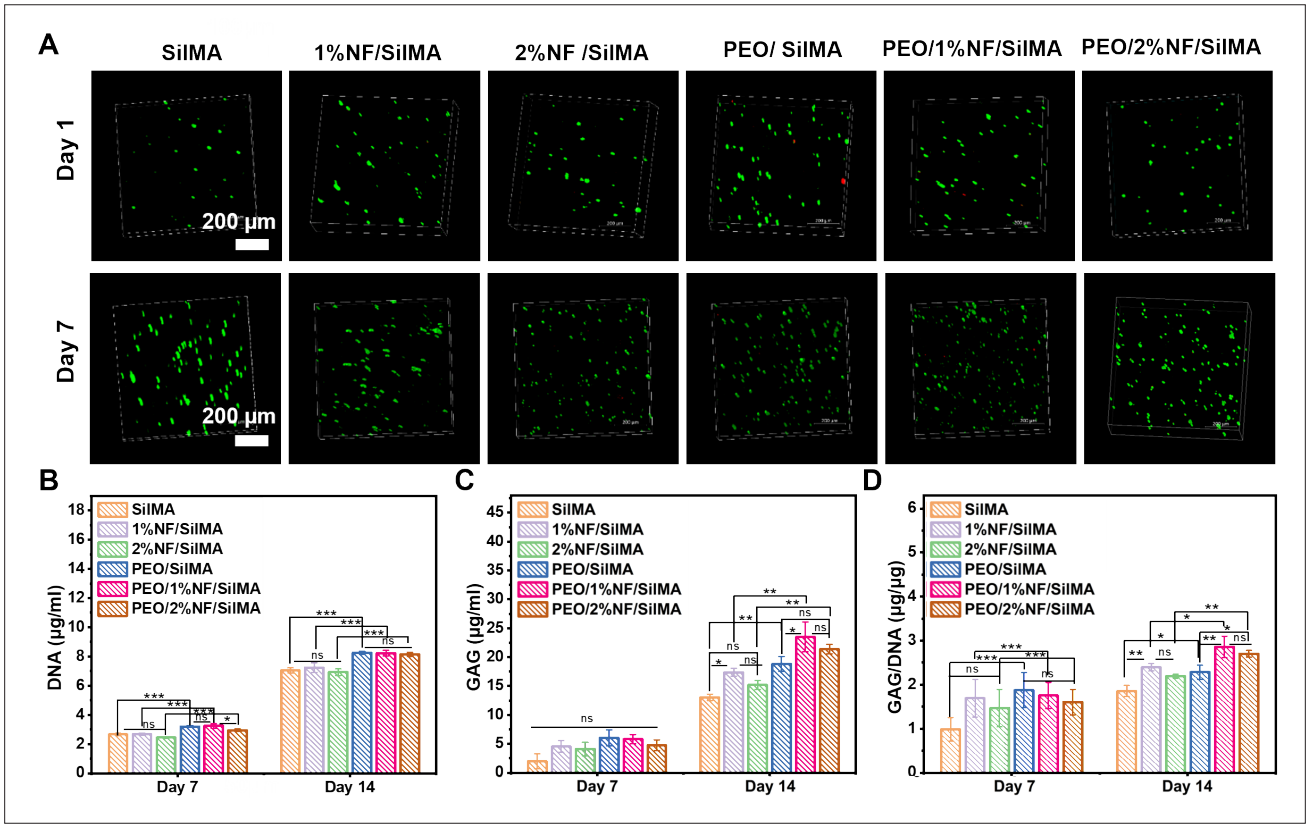

Figure 6. Cytocompatibility of the prepared hydrogel scaffolds. (A) Live/dead cell staining (green fluorescence indicates viable cells, and red fluorescence denotes dead cells). Scale bar: 200 μm; magnification: 100×. (B) DNA content. (C) GAG content. (D) GAG/DNA ratio. *Note*: Statistical significance at $^{*}p < 0.05$, $^{**}p < 0.01$, $^{***}p < 0.001$. Abbreviations: GAG, glycosaminoglycan; NF, nanofibers; ns, non-significant; PEO, poly(ethylene oxide); SilMA, silk methacryloyl.

3.4.3. Histological analysis and real-time quantitative polymerase chain rechain

Hydrogels cultured for 21 days were subjected to HE, Safranin O, and Alcian Blue staining for biocompatibility assessment. As shown in Figure 7A, ACs were distributed evenly in the hydrogels of each group and displayed relatively round morphology (HE). Safranin O (with its typical red color) and Alcian Blue densely stained the pericellular region and interterritorial matrix region, indicating a proteoglycan-rich matrix. By comparing the different groups, it was found that the number of cells in the groups modified by PEO was significantly higher. Moreover, more deposition of GAG was found in the ECM of NF-reinforced groups, especially for the PEO/1%NF/SilMA group. The results were consistent with DNA and GAG content quantification.

The RT-qPCR analysis revealed distinct gene expression profiles (Figure 7B). At Day 1, 1%NF/SilMA and 2%NF/SilMA showed comparable MKI67 (proliferation marker) levels to SilMA controls, while PEO/1%NF/SilMA and PEO/2%NF/SilMA displayed upregulated MKI67 gene expression. Compared to the groups without PEO addition, PEO-modified groups exhibited higher expression of the MKI67 gene. These results are in accordance with the live/dead staining and DNA quantification results. By Day 7, the expression of chondrogenesis-related genes was detected. The gene expression of *COL2A1*, *ACAN*, and *SOX9* decreased in non-porous NF-reinforced groups but increased significantly in PEO-modified groups. This could be due to high cell proliferation at Day 7, leading to a further decrease in the porosity and pore size of the scaffold structure. This reduction may have given rise to relatively limited nutrient transport and gas exchange within the hydrogel scaffolds, causing a decrease in the expression of chondrogenesis-related genes. However, the numerous pores induced by PEO improved this situation. The PEO/1%NF/SilMA group demonstrated the highest chondrogenic gene expression, consistent with high GAG production. SEM imaging (Figure 2C) revealed that the PEO/1%NF/SilMA hydrogels exhibited NF-attached pore walls with moderate surface roughness,

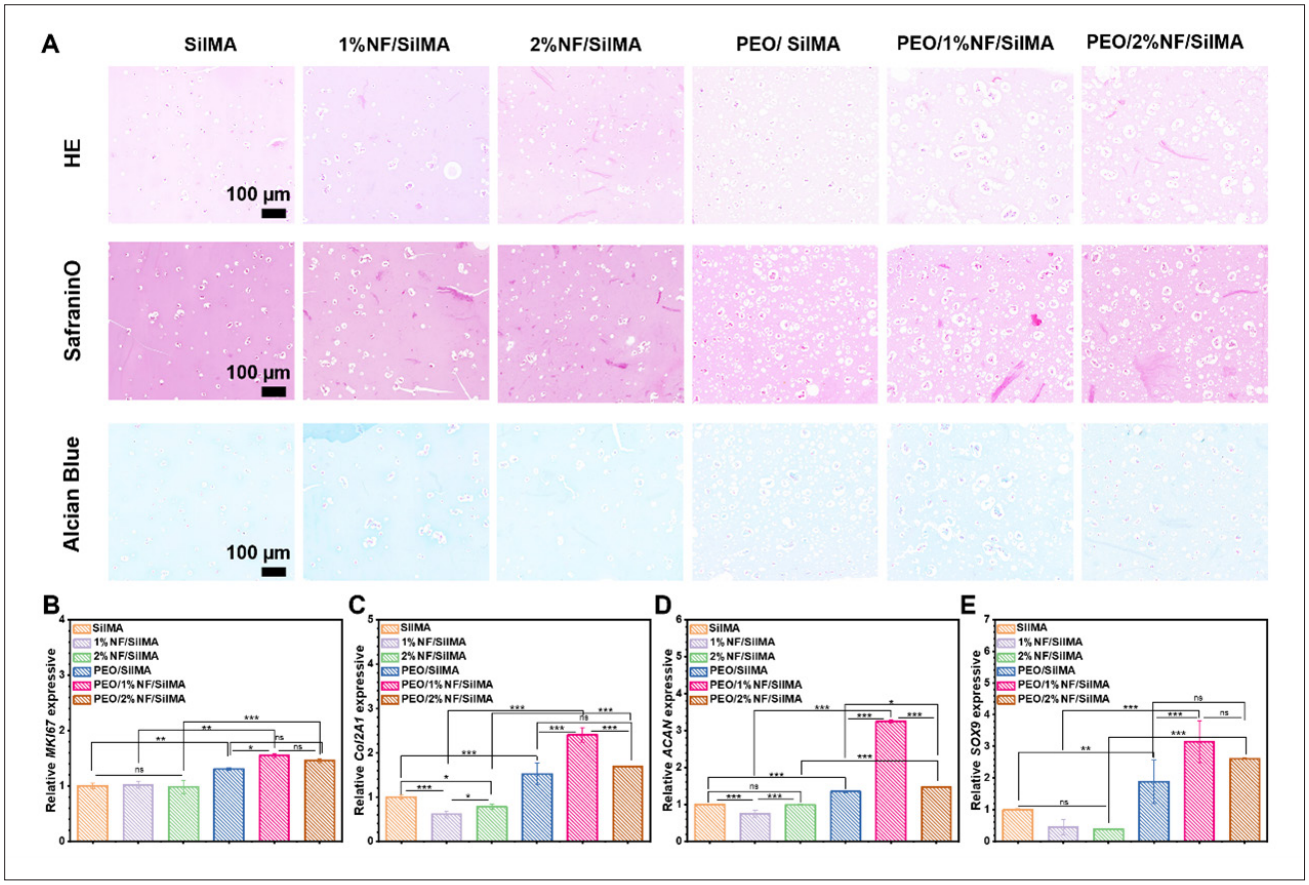

Figure 7. *In vitro* chondrogenesis effect. (A) The growth of internal cells and extracellular matrix deposition was observed by histological staining (HE, Safranin O, and Alcian Blue staining). Scale bar: 100 μm; magnification: 200×. Relative gene expression of (B) MKI67, (C) *COL2A1*, (D) *ACAN*, and (E) *SOX9* of articulator chondrocytes loaded in the prepared hydrogels. *Note*: Statistical significance at $^{*}p < 0.05$, $^{**}p < 0.01$, $^{***}p < 0.001$. Abbreviations: HE, hematoxylin and eosin; NF, nanofibers; ns, non-significant; PEO, poly(ethylene oxide); SilMA, silk methacryloyl.

which could enhance intercellular signaling and ECM secretion. In contrast, PEO/2%NF/SilMA showed irregular pits on partial pore walls due to NF aggregation, potentially impeding cell-cell communication. Previous studies demonstrated that optimized microtopographical features (e.g., wavy surfaces) significantly improved cell retention and matrix synthesis compared to flat/grooved surfaces.[51] The NF-reinforced porous groups demonstrated significantly upregulated gene expression.

3.5. Effect of *in vivo* cartilage formation

To investigate the *in vivo* cartilage formation effect of the prepared hydrogels, 3D-printed AC-laden hydrogels were implanted subcutaneously into non-obese diabetic/severe combined immunodeficiency mice, and the representative images of histological and histochemical staining are displayed in Figure 8. Compared to *in vitro* cultures, the result showed a more noticeable trend among the groups. HE staining revealed sparsely distributed cells in the SilMA, 1%NF/SilMA, and 2%NF/SilMA groups, whereas PEO-modified groups exhibited significantly increased porosity with AC clusters localized within the pores. There were large lacunae around the cells, embedded in the basophilic ECM (HE). Notably, the cartilage tissue regeneration performance of the SilMA, 1%NF/SilMA, and 2%NF/SilMA groups was similar to their *in vitro* culture result, possibly due to the limited porosity and smaller pore size. However, PEO-modified groups had visible cartilage formation in contrast with *in vitro* culture. The PEO/1%NF/SilMA group had the highest number of cells and cartilage-like structures, followed by the PEO/2%NF/SilMA and PEO/SilMA groups. Safranin O and Alcian Blue staining demonstrated positive ECM production in PEO-modified hydrogels. Col-II and Col-I immunohistochemical results correspond to the HE, Safranin O, and Alcian Blue findings. The PEO/1%NF/SilMA group exhibited increased Col-II deposition with concurrent higher Col-I accumulation than the PEO/2%NF/SilMA group.

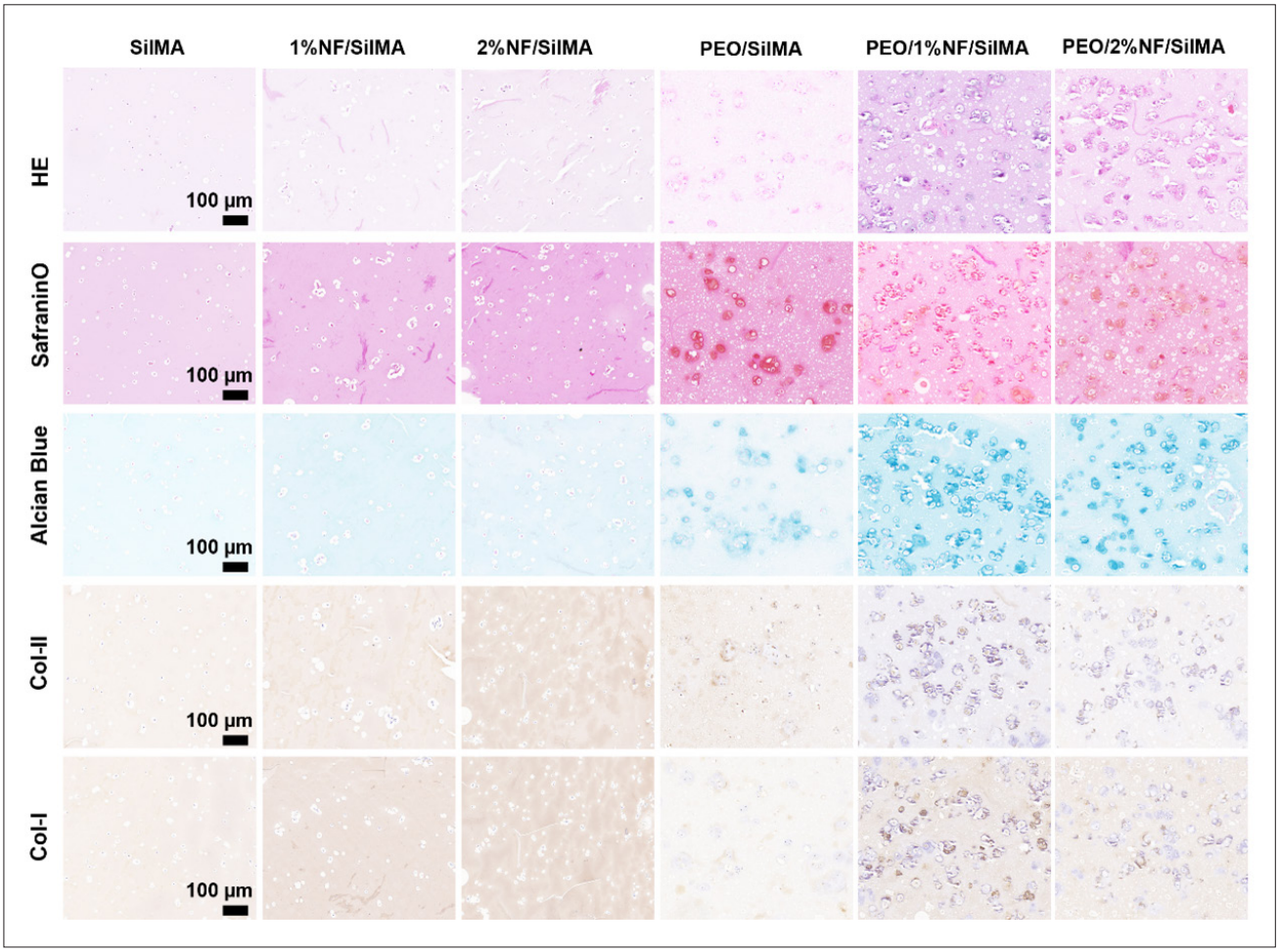

Figure 8. *In vivo* cartilage formation effect. Histological staining (HE, Safranin O, and Alcian Blue) and immunohistochemical staining images for Col-II and Col-I of each group. Scale bar: 100 μm; magnification: 200×. Abbreviations: Col I, collagen I; Col II, collagen II; HE, hematoxylin and eosin; NF, nanofibers; PEO, poly(ethylene oxide); SilMA, silk methacryloy.

As shown in Figure S7, the groups with PEO-induced porosity exhibited significantly higher Col-II and Col-I immunopositivity and average optical density compared to non-porous controls, especially for the PEO/1%NF/SilMA group. These observations coincided with the quantitative GAG measurements and chondrogenic gene expression analysis. However, due to the limitations of the animal model, these results were still unable to demonstrate which group had a better effect on cartilage formation under the weight-bearing environment. In addition, it is worth noting that the materials prepared in this study mainly contain only one type of bioactive substance, SF. This simplified composition offers a simpler system for future mechanistic studies.

4. Conclusion

This study successfully developed a dual-strategy approach for modifying 3D-printed SilMA hydrogels, combining PEO-induced porosity and NF reinforcement to enhance their cartilage tissue regeneration performance. The innovative water-in-water emulsification strategy created a porous architecture that significantly increased the average pore diameter (by over 100%) and overall porosity (75%), albeit with a significant reduction in mechanical properties. The incorporation of homogenized NFs effectively compensated for this mechanical deficit without substantially compromising porosity, while concurrently improving the 3D printability of SilMA/PEO hydrogels. Results demonstrated that the 3D printed grid-like PEO/2%NF/SilMA group had compressive strength and elastic modulus comparable to pure SilMA hydrogels but with enhanced biological functionality. Remarkably, the PEO/NF/SilMA hydrogels exhibited improved biocompatibility and marked upregulation of chondrogenic genes (*COL2A1*, *ACAN*, and *SOX9*), particularly in the PEO/1%NF/SilMA group. *In vivo* subcutaneous

implantation experiments also demonstrated the potential of SilMA/NF/PEO hydrogels in promoting cartilage tissue formation. Collectively, this novel dual-strategy approach provides a promising solution for reconciling the conflicting demands of porosity enhancement and mechanical reinforcement in cartilage tissue engineering scaffolds, achieving optimized structural and functional properties with significant potential for clinical translation.

Acknowledgments

The authors thank the Center for Scientific Research of Anhui Medical University for their valuable help in our experiment.

Funding

This research was funded by the National Natural Science Foundation of China (No. 82201034), and partially funded by Hefei Municipal Natural Science Foundation (No. 202348), Anhui Medical University Enhancement Program for Basic and Clinical Collaborative Research (No. 2022xkjT017), Anhui Provincial Institute of Translational Medicine Research Fund Project (No. 2021zhyx-C69), Anhui Medical University Graduate Research and Practice Innovation Program (No. YJS20230160).

Conflicts of interest

The authors declare they have no competing interests.

Author contributions

Conceptualization: Bingxue Xv, Xin An, Guomin Wu
Formal analysis: Bingxue Xv, Wenxin Meng, Ning Zhou
Investigation: Bingxue X,v Xin An,cYvmeng Luo
Methodology: Bingxue Xv, Guomin Wu
Writing – original draft: Bingxue Xv, Xin An
Writing – review & editing: Guomin Wu, Wenxin Meng, Ning Zhou, Yvmeng Luo

Ethics approval and consent to participate

Animal experiments were approved by the Animal Welfare Ethics Committee of the Anhui Provincial Center for Disease Control and Prevention (No.: 2024024).

Consent for publication

Not applicable.

Availability of data

All data generated or analyzed during this study are included in this published article and its supplementary information files.

References

1. Ferrari AJ, Santomauro DF, Aali A, Abate YH, Abbafati C, Murray CJL. Global incidence, prevalence, years lived with disability (YLDs), disability-adjusted life-years (DALYs), and healthy life expectancy (HALE) for 371 diseases and injuries in 204 countries and territories and 811 subnational locations, 1990–2021: a systematic analysis for the Global Burden of Disease Study 2021. *Lancet*. 2024;403(10440):2133-2161.
doi: 10.1016/s0140-6736(24)00757-8

2. Bayir E, Sahinler M, Celtikoglu MM, Sendemir A. Bioreactors in tissue engineering: mimicking the microenvironment. *Biomaterials for Organ and Tissue Regeneration*. Cambridge, UK: Elsevier. 2020:709-752.
doi: 10.1016/B978-0-08-102906-0.00018-0

3. Li Y, Li L, Li Y, Feng L, Wang B, Li G. Enhancing cartilage repair with optimized supramolecular hydrogel-based scaffold and pulsed electromagnetic field. *Bioact. Mater*. 2023;22:312-324.
doi: 10.1016/j.bioactmat.2022.10.010

4. Zhang Y, Liu X, Zeng L, Zhang J, Zuo J, Chen X. Polymer fiber scaffolds for bone and cartilage tissue engineering. *Adv Funct Mater*. 2019;29(36):1903279.
doi: 10.1002/adfm.201903279

5. Kundu, B., Rajkhowa, R., Kundu, S.C., Wang, X. Silk fibroin biomaterials for tissue regenerations. *Adv Drug Deliv Rev*. 2013;65(4):457-470.
doi: 10.1016/j.addr.2012.09.043

6. Huang K, Zhang Q-Y, Tan J, Nie R, Feng Z-Y, Xie H-Q. Accelerated cartilage regeneration through immunomodulation and enhanced chondrogenesis by an extracellular matrix hydrogel encapsulating kartogenin. *Chem Eng Jl*. 2024;497:154993.
doi: 10.1016/j.cej.2024.154993

7. Faber L, Yau A, Chen Y. Translational biomaterials of four-dimensional bioprinting for tissue regeneration. *Biofabrication*. 2023;16(1):012001.
doi: 10.1088/1758-5090/acfdd0

8. Zhang YS, Oklu R, Dokmeci MR, Khademhosseini A. Three-dimensional bioprinting strategies for tissue engineering. *Cold Spring Harb Perspect Med*. 2018;8(2):a025718.
doi: 10.1101/cshperspect.a025718

9. Li Q, Xu S, Feng Q, Dai Q, Yao L, Cao X. 3D printed silk-gelatin hydrogel scaffold with different porous structure and cell seeding strategy for cartilage regeneration. *Bioact. Mater*. 2021;6(10):3396-3410.
doi: 10.1016/j.bioactmat.2021.03.013

10. Khademhosseini A, Langer R. Microengineered hydrogels for tissue engineering. *Biomaterials*. 2007;28(34):5087-5092.
doi: 10.1016/j.biomaterials.2007.07.021

11. Gao C, Dai W, Wang X, Zhang L, Wang Y, Cai Q. Magnesium gradient-based hierarchical scaffold for dual-lineage

regeneration of osteochondral defect. *Adv Funct Mater*. 2023;33(43):2304829 .
doi: 10.1002/adfm.202304829

12. Annabi N, Nichol JW, Zhong X, et al. Controlling the porosity and microarchitecture of hydrogels for tissue engineering. *Tissue Eng Part B Rev*. 2010;16(4):371-383.
doi: 10.1089/ten.TEB.2009.0639

13. Santos MI, da Silva LCE, Bomediano MP, Catori DM, Gonçalves MC, de Oliveira MG. 3D printed nitric oxide-releasing poly(acrylic acid)/F127/cellulose nanocrystal hydrogels. *Soft Matter*. 2021;17(26):6352-6361.
doi: 10.1039/d1sm00163a

14. Shahbazi M, Jäger H, Huc-Mathis D, et al. Depletion flocculation of high internal phase pickering emulsion inks: a colloidal engineering approach to develop 3D printed porous scaffolds with tunable bioactive delivery. *ACS Appl Mater Interfaces*. 2024;16(33):43430-43450.
doi: 10.1021/acsami.4c11035

15. Li K, Shi Z, Meng Z. Study on the foam properties of peanut oil body (POB)-based oil-in-water-in-oil (O/W/O) foamed emulsion gel: the key role played by the interface between the water phase and the outer oil phase. *Food Chem*. 2025;464:141663.
doi: 10.1016/j.foodchem.2024.141663

16. Frith WJ. Mixed biopolymer aqueous solutions-phase behaviour and rheology. *Adv Colloid Interface Sci*. 2010;161(1-2):48-60.
doi: 10.1016/j.cis.2009.08.001

17. Ying GL, Jiang N, Maharjan S, Yin YX, Chai RR, Zhang YS. Aqueous two-phase emulsion bioink-enabled 3D bioprinting of porous hydrogels. *Adv Mater*. 2018;30(50):1805460.
doi: 10.1002/adma.201805460

18. Wang L-S, Du C, Toh WS, Wan ACA, Gao SJ, Kurisawa M. Modulation of chondrocyte functions and stiffness-dependent cartilage repair using an injectable enzymatically crosslinked hydrogel with tunable mechanical properties. *Biomaterials*. 2014;35(7):2207-2217.
doi: 10.1016/j.biomaterials.2013.11.070

19. Zhou Y, Liang K, Zhao S, Zhan C, Li J, Xiao P. Photopolymerized maleilated chitosan/methacrylated silk fibroin micro/nanocomposite hydrogels as potential scaffolds for cartilage tissue engineering. *Int J Biol Macromol*. 2018;108:383-390.
doi: 10.1016/j.ijbiomac.2017.12.032

20. Kim SH, Yeon YK, Lee JM, Chao JR, Lee Y, Park CH. Precisely printable and biocompatible silk fibroin bioink for digital light processing 3D printing. *Nat Commun*. 2018;9(1):1620.
doi: 10.1038/s41467-018-03759-y

21. Zhang Q, Lu H, Kawazoe N, Chen G. Pore size effect of collagen scaffolds on cartilage regeneration. *Acta Biomater*. 2014;10(5):2005-2013.
doi: 10.1016/j.actbio.2013.12.042

22. Ying G, Jiang N, Parra-Cantu C, Tang G, Zhang J, Zhang YS. Bioprinted injectable hierarchically porous gelatin methacryloyl hydrogel constructs with shape-memory properties. *Adv Funct Mater*. 2020;30(46):2003740.
doi: 10.1002/adfm.202003740

23. Wang C, Su Y, Xie J. Advances in electrospun nanofibers: versatile materials and diverse biomedical applications. *Acc Mater Res*. 2024;5(8):987-999.
doi: 10.1021/accountsmr.4c00145

24. Huang T, Zeng Y, Li C, Zhou Z, Xu J, Wang K. Application and development of electrospun nanofiber scaffolds for bone tissue engineering. *ACS Biomater Sci Eng*. 2024;10(7):4114-4144.
doi: 10.1021/acsbiomaterials.4c00028

25. Long M, Wu G, Tao F, Ma S, Dong X, Deng H. Nanofibrous textured silk aerogel with 3D channel arrays and adjustable mechanical properties for bone tissue regeneration. *Int J Biol Macromol*. 2024;278(Pt 2):134372.
doi: 10.1016/j.ijbiomac.2024.134372

26. Song Y, Shimanovich U, Michaels TCT, et al. Fabrication of fibrillosomes from droplets stabilized by protein nanofibrils at all-aqueous interfaces. *Nat Commun*. 2016;7(1):12934.
doi: 10.1038/ncomms12934

27. Rockwood DN, Preda RC, Yücel T, Wang X, Lovett ML, Kaplan DL. Materials fabrication from *Bombyx mori* silk fibroin. *Nat Protoc*. 2011;6(10):1612-1631.
doi: 10.1038/nprot.2011.379

28. Ma X, Wu G, Dai F, et al. Chitosan/polydopamine layer by layer self-assembled silk fibroin nanofibers for biomedical applications. *Carbohydr Polym*. 2021;251:117058.
doi: 10.1016/j.carbpol.2020.117058

29. Nicolai T, Murray B. Particle stabilized water in water emulsions. *Food Hydrocoll*. 2017;68:157-163.
doi: 10.1016/j.foodhyd.2016.08.036

30. Sawyer Mt, Eixenberger J, Nielson O, Manzi J, Francis C, Estrada D. Correlative imaging of three-dimensional cell culture on opaque bioscaffolds for tissue engineering applications. *ACS Appl Biomater*. 2023;6(9):3717-3725.
doi: 10.1021/acsabm.3c00408

31. Yoon J, Han H, Jan J. Nanomaterials-incorporated hydrogels for 3D bioprinting technology. *Nano Converg*. 2023;10(1):52.
doi: 10.1186/s40580-023-00402-5

32. Chang A, Babhadiashar N, Barrett-Catton E, Asuri P. Role of nanoparticle-polymer interactions on the development of double-network hydrogel nanocomposites with high mechanical strength. *Polymers*. 2020;12(2):470.
doi: 10.3390/polym12020470

33. Cheng Y, Cheng G, Xie C, Yin C, Dong X, Li Z. Biomimetic silk fibroin hydrogels strengthened by silica nanoparticles distributed nanofibers facilitate bone repair. *Adv Healthc Mater*. 2021;10(9):2001646.
doi: 10.1002/adhm.202001646

34. Lee J, Sultan M, Kim S, et al. Artificial auricular cartilage using silk fibroin and polyvinyl alcohol hydrogel. *Int J Mol Sci*. 2017;18(8):1707.
doi: 10.3390/ijms18081707

35. Karageorgiou V, Kaplan D. Porosity of 3D biomaterial scaffolds and osteogenesis. *Biomaterials*. 2005;26(27):5474-5491.
doi: 10.1016/j.biomaterials.2005.02.002

36. Lutzweiler G, Ndreu Halili A, Engin Vrana N. The overview of porous, bioactive scaffolds as instructive biomaterials for tissue regeneration and their clinical translation. *Pharmaceutics*. 2020;12(7):602.
doi: 10.3390/pharmaceutics12070602

37. Navaei A, Saini H, Christenson W, Sullivan RT, Ros R, Nikkhah M. Gold nanorod-incorporated gelatin-based conductive hydrogels for engineering cardiac tissue constructs. *Acta Biomater*. 2016;41:133-146.
doi: 10.1016/j.actbio.2016.05.027

38. Chen S, Lei T, Zhang Y, Wu H, He S, Liu Y. Nanofiber induced silk fibroin nanofiber/silk fibroin (SFNF/SF) fibrous scaffolds for 3D cell culture. *Fibers Polym*. 2023;24(2):433-444.
doi: 10.1007/s12221-023-00113-y

39. Wang C-C, Yan K-C, Lin K-H, Liu H-C, Lin F-H. A highly organized three-dimensional alginate scaffold for cartilage tissue engineering prepared by microfluidic technology. *Biomaterials*. 2011;32(29):7118-7126.
doi: 10.1016/j.biomaterials.2011.06.018

40. Jia L, Zhang Y, Yao L, Zhang P, Ci Z, Zhou G. Regeneration of human-ear-shaped cartilage with acellular cartilage matrix-based biomimetic scaffolds. *Appl Mater Today*. 2020;20:100639.
doi: 10.1016/j.apmt.2020.100639

41. O'Brien FJ, Harley BA, Yannas IV, Gibson LJ. The effect of pore size on cell adhesion in collagen-GAG scaffolds. *Biomaterials*. 2005;26(4):433-441.
doi: 10.1016/j.biomaterials.2004.02.052

42. Im GI, Ko JY, Lee JH. Chondrogenesis of adipose stem cells in a porous polymer scaffold: influence of the pore size. *Cell Transplant*. 2012;21(11):2397-2405.
doi: 10.3727/096368912X638865

43. Sheng R, Chen J, Wang H, Luo Y, Liu J, Zhang W. Nanosilicate-reinforced silk fibroin hydrogel for endogenous regeneration of both cartilage and subchondral bone. *Adv Healthc Mater*. 2022;11(17):e2200602.
doi: 10.1002/adhm.202200602

44. Braxton T, Lim K, Alcala-Orozco C, et al. Mechanical and physical characterization of a biphasic 3D printed silk-infilled scaffold for osteochondral tissue engineering. *ACS Biomater Sci Eng*. 2024;10(12):7606-7618.
doi: 10.1021/acsbiomaterials.4c01865

45. Li H, Li J, Yu S, Wu C, Zhan W. The mechanical properties of tibiofemoral and patellofemoral articular cartilage in compression depend on anatomical regions. *Sci Rep*. 2021;11(1):6128.
doi: 10.1038/s41598-021-85716-2

46. Jin R, Xu B, Guo D, et al. Advanced chemical modification technology of inorganic oxide nanoparticles in epoxy resin and mechanical properties of epoxy resin nanocomposites: a review. *Nano Mater Sci*. 2024;18(8);1707.
doi: 10.3390/ijms18081707

47. Shao C, Li Y, Chi J, Ye F, Zhao Y. Hierarchically inverse opal porous scaffolds from droplet microfluidics for biomimetic 3D cell co-culture. *Engineering*. 2021;7(12):1778-1785.
doi: 10.1016/j.eng.2020.06.031

48. Luo B, Wang S, Song X, Chen S, Qi Q, You Z. An encapsulation-free and hierarchical porous triboelectric scaffold with dynamic hydrophilicity for efficient cartilage regeneration. *Adv Mater*. 2024;36(27):2401009.
doi: 10.1002/adma.202401009

49. Chen Y, Mehmood K, Chang Y-F, Tang Z, Li Y, Zhang H. The molecular mechanisms of glycosaminoglycan biosynthesis regulating chondrogenesis and endochondral ossification. *Life Sci*. 2023;335:122243.
doi: 10.1016/j.lfs.2023.122243

50. Jia L, Hua Y, Zeng J, Liu W, Wang D, Jiang H. Bioprinting and regeneration of auricular cartilage using a bioactive bioink based on microporous photocrosslinkable acellular cartilage matrix. *Bioact Mater*. 2022;16:66-81.
doi: 10.1016/j.bioactmat.2022.02.032

51. Bettahalli NMS, Arkesteijn ITM, Wessling M, Poot AA, Stamatialis D. Corrugated round fibers to improve cell adhesion and proliferation in tissue engineering scaffolds. *Acta Biomater*. 2013;9(6):6928-6935.
doi: 10.1016/j.actbio.2013.02.029